THE ISOTHERMAL OUTFLOW IN THE MASSIVE STAR-FORMING REGION G240.31+0.07

Junhao Liu,[1] Keping Qiu,[1,2] Friedrich Wyrowski,[3] Karl Menten,[3] Rolf Güsten,[3] Yue Cao,[1] and Yuwei Wang[1]

[1]School of Astronomy and Space Science, Nanjing University, 163 Xianlin Avenue, Nanjing 210023, P.R.China
[2]Key Laboratory of Modern Astronomy and Astrophysics (Nanjing University), Ministry of Education, Nanjing 210023, P.R.China
[3]Max-Planck-Institut für Radioastronomie, Auf dem Hügel 69, 53121 Bonn, Germany

ABSTRACT

We present Atacama Pathfinder Experiment (APEX) observations toward the massive star-forming region G240.31+0.07 in the CO 3-2 [J = 3-2], 6-5, and 7-6 lines. We detect a parsec-sized, bipolar, and high velocity outflow in all the lines, which allow us, in combination with the existing CO 2-1 data, to perform a multi-line analysis of physical conditions of the outflowing gas. The CO 7-6/6-5, 6-5/3-2, and 6-5/2-1 ratios are found to be nearly constant over a velocity range of $\sim 5 - 25$ km s^{-1} for both blueshifted and redshifted lobes. We carry out rotation diagram and large velocity gradient (LVG) calculations of the four lines, and find that the outflow is approximately isothermal with a gas temperature of 50 K, and that the the CO column density clearly decreases with the outflow velocity. If the CO abundance and the velocity gradient do not vary much, the decreasing CO column density indicates a decline in the outflow gas density with velocity. By comparing with theoretical models of outflow driving mechanisms, our observations and calculations suggest that the massive outflow in G240.31+0.07 is being driven by a wide-angle wind and further support a disk mediated accretion at play for the formation of the central high-mass ~~type~~ star.

Keywords: ISM: individual objects (G240.31+0.07) - ISM: jets and outflows - stars: formation

1. INTRODUCTION

Bipolar molecular outflows, mostly observed ~~via~~ [in rotational transitions of] CO, SiO, ~~HCO$^\pm$~~ and ~~their isotopes~~ [some other molecules], are a common phenomenon associated with young stellar objects (YSOs) of all masses (Zhang et al. 2001; Beuther et al. 2002a; Wu et al. 2004, 2005; Maud et al. 2015). It is believed that molecular outflows trace the accretion-powered ejections in sites of low-mass star formation, and they play an important role in the star formation process by significant impacts on the surrounding material and the parent cloud. Although molecular outflows have been ~~well studied~~ [extensively observed], their driving mechanism remains unknown. Molecular outflows from low-mass YSOs were thought to be produced by the interaction between wide-angle winds and ambient gas (Shu et al. 1991; Lee et al. 2001), or by jet bow shocks (Raga & Cabrit 1993; Masson & Chernin 1993; Lee et al. 2001). Although the wind-driven model and the jet-driven model can both explain some observed outflow features, none of them are capable of producing all of the observed features of different types of outflows (Lee et al. 2000, 2002). Two-component models with both highly collimated jet and wide-angle wind were then developed to establish a unified picture of the observed outflow features(Shu et al. 2000; Banerjee & Pudritz 2006; Pudritz et al. 2006; Shang et al. 2006; Pudritz et al. 2007; Machida et al. 2008).

Massive molecular outflows, which are associated with high-mass YSOs, are less understood than their low-mass counterparts. Due to the rarity and typically large distances, there are few studies towards outflows driven by massive YSOs. Although observations have shown that the morphology and kinematics of some massive outflows are very similar to what is observed for those driven by low-mass YSOs (Shepherd et al. 1998; Beuther et al. 2002b; Qiu et al. 2009; Ren et al. 2011), extremely collimated outflows and circumstellar disks have remained elusive for sources more massive than those equivalent to early B-type stars (Arce et al. 2007). And there is little theoretical work on modeling outflows from high-mass YSOs. Many questions, e.g., how the outflows from massive YSOs are accelerated, how they differ from low-mass outflows, and how they affect the high-mass star-forming processes, are still unanswered. ~~It is essen-~~

Corresponding author: Keping Qiu
kpqiu@nju.edu.cn

~~tial to address these questions by studying more outflows associated with high-mass star-forming regions.~~

Most previous studies of outflows have used low-J rotational transitions of CO (transitions up to $J_u = 3$, with upper-state energies E_u up to 30 K), which are readily easily excited at low temperatures and can be ~~easily~~ observed by ground-based facilities, to characterize the morphology and kinematics of the relatively cold and extended molecular gas ~~in morphology and kinematics~~. Due to the Earth's atmosphere, mid-J CO lines (referring to CO 6-5 and CO 7-6 throughout this paper, with E_u up to 150 K), which are less affected by ambient gas, are not commonly observed. In several studies, mid-J CO transitions have been reported to trace the warm gas (T > 50 K) in outflows of low-mass and intermediate-mass YSOs (van Kempen et al. 2009a,b; Yıldız et al. 2012; van Kempen et al. 2016). By comparing multi-line CO observations (both low-J and mid-J) with the results of radiative transfer models, the physical properties (temperature, gas density and CO column density) of the outflowing gas could be ~~well~~ better constrained (Lefloch et al. 2015).

This paper is a follow-up study of the G240.31+0.07 (hereafter G240) outflow (Qiu et al. 2009). We report the 12-m submillimeter Atacama Pathfinder Experiment Telescope[1] (APEX) observations of G240, an active high-mass star-forming region associated with IRAS 07427-2400 and located at a distance of ~5.4 kpc (Choi et al. 2014; Sakai et al. 2015). It harbors an ultracompact HII region and is associated with OH and H_2O masers (Hughes & MacLeod 1993; Caswell 1997; MacLeod et al. 1998; Migenes et al. 1999; Caswell 2003). Its far-infrared luminosity of $10^{4.7}$ $L_\odot$ is consistent with a spectral type O8.5 zero-age main-sequence star (MacLeod et al. 1998). ~~Qiu et al. (2009) presented a high-resolution interferometric study at 1.3 mm and resolved the central part of G240 into three dusty cores MM1, MM2, and MM3.~~ Kumar et al. (2003) mapped the CO 3-2 emission with a 20″ beam ~~and found a prominent bipolar outflow at a position angle (PA) of 132° and a weaker component at PA ~ 101°~~. From $C^{18}O$ 2-1 observations, Kumar et al. (2003) found the cloud velocity (v_{cloud}) with respect to the local standard of rest to be ~ 67.5 km s^{-1}. ~~Recently,~~ Qiu et al. (2009) presented a detailed ~~single-dish and interferometric~~ high resolution study of ^{12}CO 2-1 and ^{13}CO 2-1 emissions and detected a bipolar, wide-angle, quasi-parabolic molecular outflow. Li et al. (2013) theoretically interpreted the G240 outflow

as a result from interaction between the wind and the ambient gas in the form of turbulent entrainment. ~~In addition,~~ Recently Qiu et al. (2014) reported the detection of an hourglass magnetic field aligned within 20° of the outflow axis.

In this paper, we present a CO multi-transition (2-1, 3-2, 6-5, 7-6) study towards the G240 outflow. With rotation diagram (RD) analysis and large velocity gradient (LVG) calculations, we estimate the physical parameters of the outflow as functions of gas velocity. We then discuss the results of the analysis.

2. OBSERVATIONS

The observations were performed with the 12 m APEX telescope. The APEX CO (6-5) and CO (7-6) observations were performed in 2010 July with the Carbon Heterodyne Array of the MPIfR (CHAMP+) (Kasemann et al. 2006). The APEX CO (3-2) observations were made in 2011 October using the First Light APEX Submillimeter Heterodyne (FLASH) receiver (Heyminck et al. 2006).

Pointings were checked by comparing these lines with the CO 2-1 data adopted from Qiu et al. (2009), and were found to be within ~ 7″ for CO 3-2 and within ~ 4″ for CO 6-5 and 7-6. The system temperatures were found to be ? at ? GHz. The ? spectrometer was used as the backend with a resolution of ? kHz (? km s^{-1}). The data were smoothed to 2 km s^{-1}, then the rms noises in the spectra in the central part of the map are of the order 0.03-0.05 K at 345 GHz, 0.15-0.25 K at 691 GHz and 0.40 - 0.60 K at 809 GHz at the central region of the maps. Noises are higher at the edge of the maps. Beam efficiencies, determined by observations of planets, were 0.65, 0.41 and 0.40 at 345 GHz, 691 GHz and 809 GHz, respectively. The APEX beam sizes are ~ 19″ at 345 GHz, ~ 9″ at 691 GHz and ~ 8″ at 809 GHz. Calibration uncertainties were assumed to be 15 %, 20% and 30% at 345 GHz, 691 GHz and 809 GHz, relatively. These data were complemented with the perviously observed combined data from the Submillimeter Array[2] (SMA) and the Caltech Submillimeter Observatory[3] (CSO) 10.4 m telescope in CO 2-1 (Qiu et al. 2009). The CO 2-1 data has a calibration uncertainty of 10 %, with the rms estimated to be 0.06-0.10 K in 2 km s^{-1} channels. Table 1 shows a summary of the line informations.

---

[1] The Atacama Pathfinder Experiment Telescope is a collaboration between the Max-Planck-Institut für Radioastronomie, the European Southern Observatory, and the Onsala Space Observatory.

[2] The Submillimeter Array is a joint project between the Smithsonian Astrophysical Observatory and the Academia Sinica Institute of Astronomy and the Astrophysics and is funded by the Smithsonian Institution and the Academia Sinica.

[3] The Caltech Submillimeter Observatory was supported by the NSF grant AST-0229008 and was decommissioned in 2015.

Table 1. Line informations

Line	Frequency	Beam size	σ_{cal} [a]	σ_{rms} [b]	η_s [c]
	GHz	″	%	K	
CO 2-1	230.5380	3.93×3.10[d]	10	0.08	–
CO 3-2	345.7960	19.16	15	0.04	0.65
CO 6-5	691.4731	9.49	20	0.20	0.41
CO 7-6	806.6518	8.12	30	0.50	0.40

[a] Calibration error.

[b] Average rms in 2 km s^{-1} channels.

[c] Beam efficiency.

[d] Major axis × minor axis.

3. RESULTS

3.1. CO emission maps

The CO 3-2, 6-5 and 7-6 emissions are detected (with obvious outflow signatures and with peak intensities > 2 σ_{rms}) in velocity ranges from 42 km s^{-1} to 94 km s^{-1}, 44 km s^{-1} to 92 km s^{-1}, and 46 km s^{-1} to 90 km s^{-1}, respectively. Figure 1 shows the integrated low-velocity (LV) and high-velocity (HV) emissions of the four lines. The velocity ranges chosen to highlight the LV and HV components of the outflowing gas follow those in Qiu et al. (2009), except that the channels with no detections were excluded for the HV component. The morphologies of the bipolar outflow seen in the emission from the CO 3-2, 6-5 and 7-6 lines are very similar. Due to the coarser angular resolution, the wide-angle structure seen in the higher resolution CO 2-1 image is not seen in the CO 3-2, 6-5, 7-6 maps.

3.2. Physical conditions of the outflow

3.2.1. Methodology

The physical conditions of the outflow can be constrained by comparing the observed line intensities with the results of statistical-equilibrium calculations. To study the four lines at the same spatial resolution, the CO 2-1, 6-5 and 7-6 maps were reconstructed with the same beam of the CO 3-2 map. The average rms noise levels are ~0.004 K, ~0.04 K and ~0.1 K for the convolved CO 2-1, 6-5 and 7-6 data, respectively. For both lobes of the outflow, the CO line intensities were measured at roughly the peak positions of the HV components of the convolved CO maps (marked as two crosses in every panel of Figure 1), and were then used in the following analysis. Figure 2 shows the ratios of the main-beam brightness temperatures (T_{mb}) of different

CO lines as functions of velocity. The CO 7-6/6-5, 6-5/3-2, and 6-5/2-1 ratios are remarkably constant over a velocity range of $\sim 5 - 25$ km s^{-1} with respect to the cloud velocity. In the analysis, we only used channels of ≤ 60 km s^{-1} and ≥ 74 km s^{-1} to avoid contaminations from the ambient gas, and we excluded channels of < 46 km s^{-1} or > 90 km s^{-1} because of their low signal-to-noise ratios. The outflow emission was analyzed in each 2 km s^{-1} bin. Considering that the ^{13}CO 2-1 emission was only marginally detected in the outflowing gas with high sensitivity observations (Qiu et al. 2009), we assumed the four ^{12}CO lines to be optically thin. In the optically thin case, the source size is degenerate with column density (see section 4.2). We didn't correct the observed line intensities for beam filling factors, so the derived CO column densities should be considered as beam-averaged values. In the calculation, errors on line intensities took into account both the calibration error and the rms noise.

3.2.2. Rotation diagram analysis

Firstly, we performed a simple rotation diagram (RD) analysis (Goldsmith & Langer 1999) to estimate the excitation conditions of the outflowing gas under the assumption of local thermal equilibrium (LTE). The population of each energy level is given by

$$N_{up} = \frac{N_{CO}}{Z} g_{up} e^{-E_{up}/kT_{kin}}, \tag{1}$$

where N_{up} is the column density in the upper state, g_{up} the statistical weight of the upper state, E_{up} the upper energy level, k the Boltzmann constant, and Z is the partition function. The rotation diagram for CO at 84 km s^{-1} is shown in Figure 3 as an example. The different energy levels are well reproduced by a single-component, indicating that the four transitions are probing the same volume of gas. Similar rotation diagram patterns with one gas component are found at other velocities. The derived gas temperature and CO column density as functions of the gas velocity are shown in Figure 5.

3.2.3. Large velocity gradient analysis

Secondly, the non-LTE radiative transfer code RADEX (van der Tak et al. 2007) was used to better constrain the gas density (n), the kinetic temperature (T) and the CO column density (N) of the outflowing gas. RADEX employs the the LVG approximation. We built a large grid of LVG models varying the three parameters (n, T and N), and obtained the best fitting results by minimizing the χ^2 calculated from the observed intensities and the model intensities. With four lines observed and three parameters to constrain, our fitting had one degree of freedom. In Figure 4, the fitting results at 84 km s^{-1}
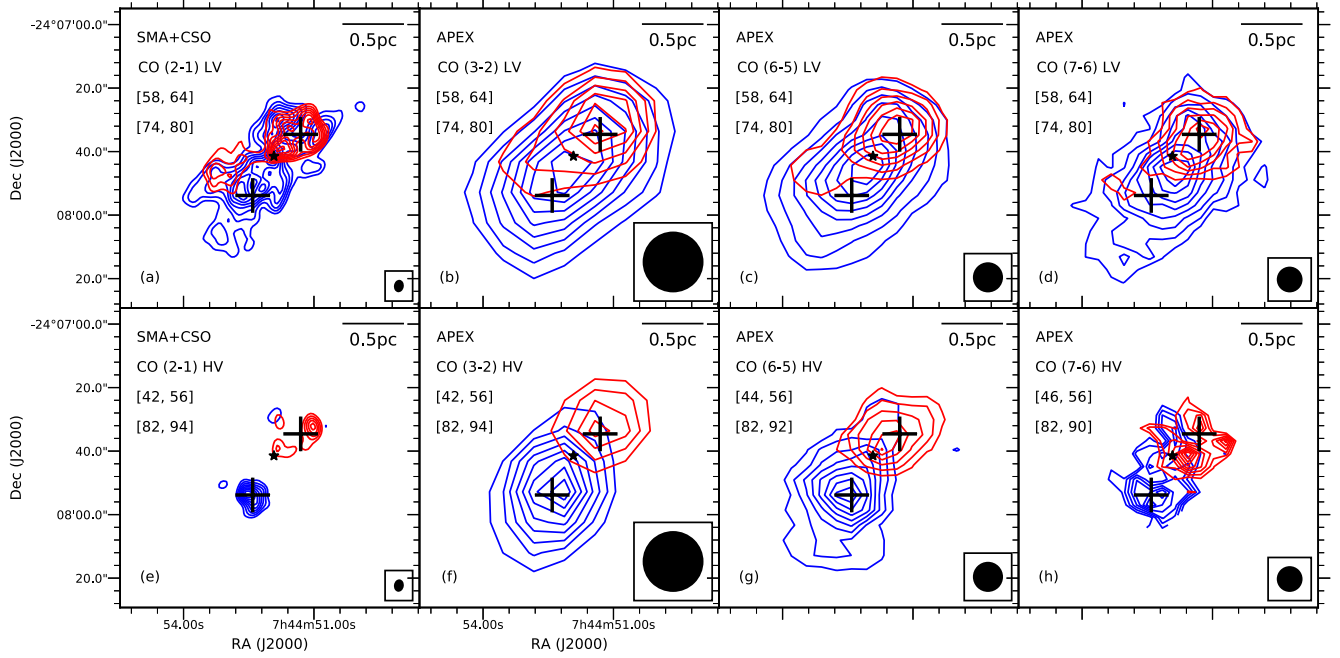
Figure 1. (a)-(d) Low-velocity CO J = 2-1, 3-2, 6-5, 7-6 emissions, integrated from 58 to 64 km s^{-1} for the blueshifted lobe (blue) and from 74 to 80 km s^{-1} for the redshifted lobe (red); (e)-(f) High-velocity CO J = 2-1, 3-2 emissions, integrated from 42 to 56 km s^{-1} for the blueshifted lobe (blue) and from 82 to 94 km s^{-1} for the redshifted lobe (red); (g) High-velocity CO J = 6-5 emission, integrated from 44 to 56 km s^{-1} for the blueshifted lobe (blue) and from 82 to 92 km s^{-1} for the redshifted lobe (red) (h) High-velocity CO J = 7-6 emission, integrated from 46 to 56 km s^{-1} for the blueshifted lobe (blue) and from 82 to 90 km s^{-1} for the redshifted lobe (red). For (a)-(g), the contour levels start from 20% and continue at steps of 10% of the peak emission. For (h), the contour levels start from 30% and continue at steps of 10% of the peak emission. Edge channels are masked out because of high noise levels. The black star marks the position of a H$_2$O maser spot which is associated with IRAS 07427-2400 (Sakai et al. 2015). The beam of each observational dataset is shown in the lower right corner of each panel.
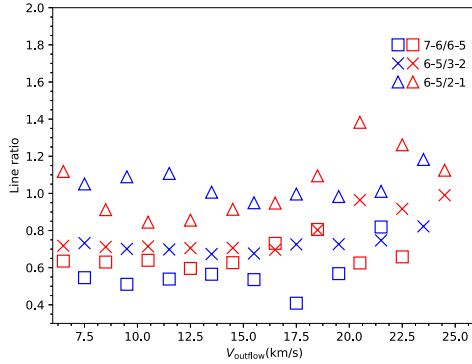
Figure 2. Ratios of the main-beam brightness temperatures of different CO lines at different velocities. Blue symbols denote the measurements from the blueshifted lobe, and red symbols the redshifted lobe. The V_{outflow} shown here is related to the cloud velocity v_{cloud} by the relation: $V_{\text{outflow}} = | v_{\text{outflow}} - v_{\text{cloud}} |$, where v_{outflow} is the outflow velocity with respect to the local standard of rest.
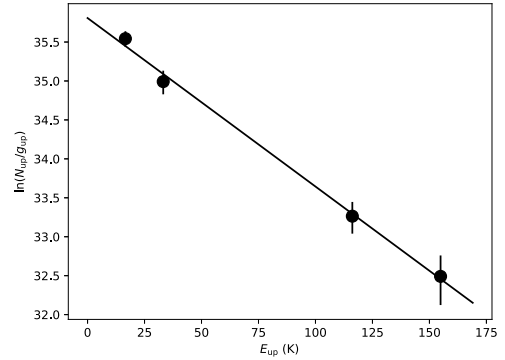

Figure 3. A rotation diagram for CO at 84 km s^{-1}. The fitted line shows the Boltzmann distribution of the rotational populations. The line represents a rotational temperature of 48.5 K and a total column density of 2.0×10^{15} cm^{-2}. The black solid circles show the data with error bars.

are shown ~~as examples of the distributions of χ^2~~. Only one minimum of χ^2 is found in the $[T, N]$ plane. In the $[T, n]$ and $[n, N]$ planes, the χ^2 distributions show

Figures 4(a) and 4(b) show that the gas temperature is well constrained to ~50 K. In Figures 4(b) and 4(c), the CO column density is stringently constrained to 2.2 × 10^15 cm^–2. The χ2 distributions in Figures 4(a) and 4(c) indicate that in the best LVG models, the gas density is high enough to thermalize the emissions, and thus only lower limits of the gas density could be derived from χ2 minimization. This implies that the LTE assumption adopted by the above RD analysis is valid, and hence we obtain similar gas temperatures and CO column densities from the RD and LVG analyses.

(a)

(b)

(c)
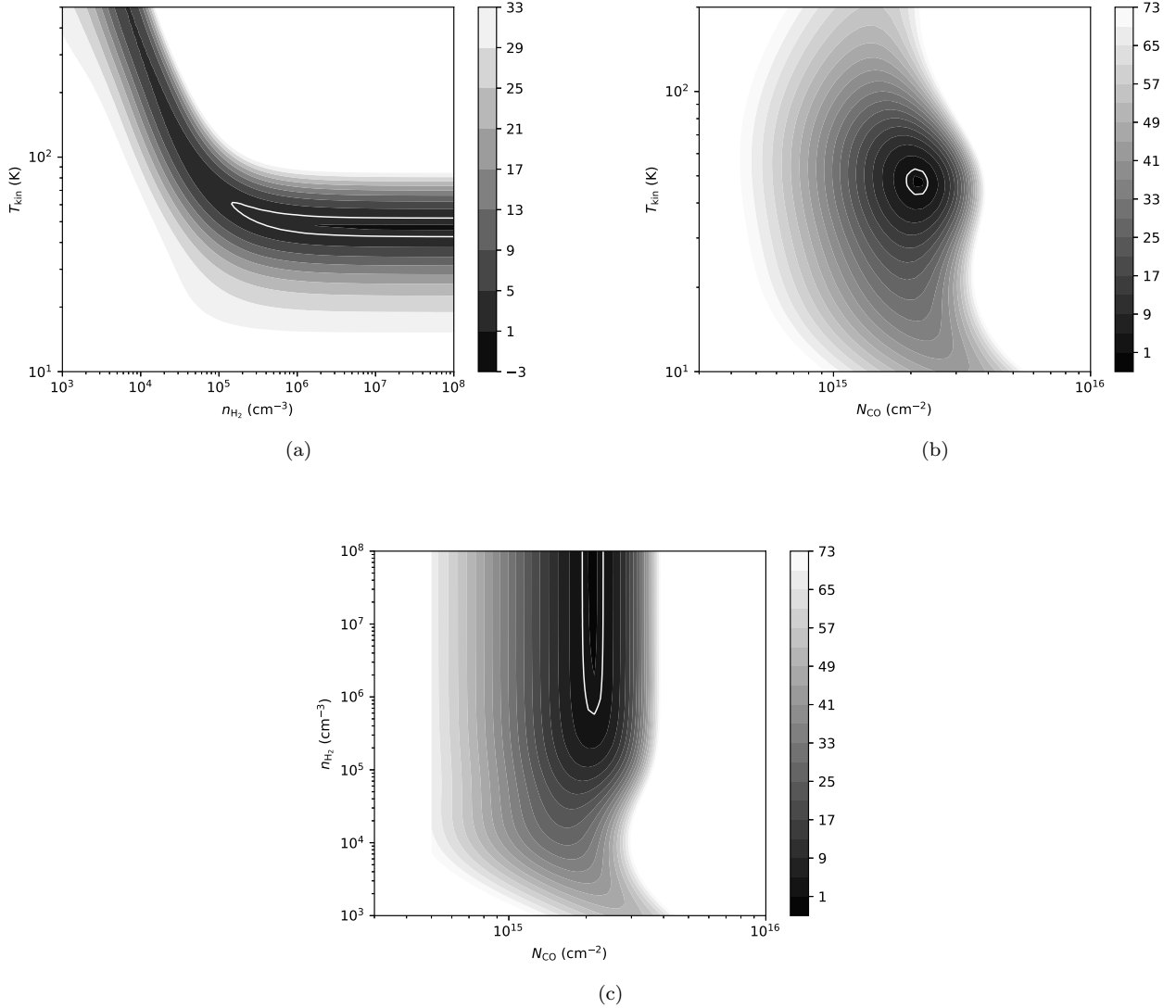
Figure 4. (a)-(c) The χ^2 distribution at 84 km s^{-1} in the $[T, n]$, $[T, N]$ and $[n, N]$ planes, with the third parameter fixed to the value of the best fitting result at this velocity. The lower limit of gas density is 1.8×10^5 cm^{-3}. The best-fit solution is obtained for $T = 46.1$ K and N $= 2.2 \times 10^{15}$ cm^{-2}. The $\chi^2_{\rm red}$ of the best-fit solution is 1.00. The Solid white contours show the 1σ confidence levels.

that the gas is thermalized and no upper limits to the H$_2$ density could be derived, which confirms the LTE assumption of the rotation diagram analysis. Similar χ^2 distribution patterns were found at other velocities. ~~The best fit solutions at different velocities are very close to the results of the rotation diagram (see Figure 5).~~ The reduced χ^2 ($\chi^2_{\rm red}$) of the best fitting results varies from 0.10 to 1.72 at different velocities. We derive the uncertainties of each parameter from the 1σ confidence region in the 3D parameter space at the velocities where $\chi^2_{\rm red} \sim 1$ as the representative parameter uncertainties. The uncertainty of CO column densities is ~ 10 %. The 1σ confidence range of the temperature is about 40 ~~K~~

relative

The temperature is found in the range of

~ 60 K. And the gas density is $> 10^5$ cm^{-3} over the entire outflow. The modeling results also predict that the four transitions are optically thin in the outflowing gas~~, which is consistent with our assumptions~~. Figure A1 shows the comparison of the observed CO intensities with the LVG modeling results in each velocity bin.

velocity range

3.2.4. *T-V and N-V relations*

In Figure 5, the T-V diagram shows that the gas is approximately isothermal with a gas temperature of $\sim$ 50 K, while the N-V diagram shows that the CO column density ~~in each 2 km s^{-1} bin~~ decreases from $\sim 2 \times 10^{16}$ cm^{-2} at $\sim \pm 7$ km s^{-1} down to $\sim 4 \times 10^{14}$ cm^{-2} at $\sim \pm$

The variation of the physical conditions of the outflowing gas as a function of velocity is of great interests to our understanding of the driving mechanism of the outflow. With the RD and LVG analyses we have estimated the gas temperature, density, and CO column density at different velocities. Figure 5 shows the temperature-velocity (T-V) and CO column density-velocity (N-V) relations.

(handwritten margin note in red, top): 总的来说，从Discussion开始，内容太薄弱（不如对前人和他人工作的讨论该详细的时候不详细，都是一句带过，这应该是调研），逻辑性不强（没有对句子到段落间的严密关系和因果关系等细加推敲）。

(a)

(b)
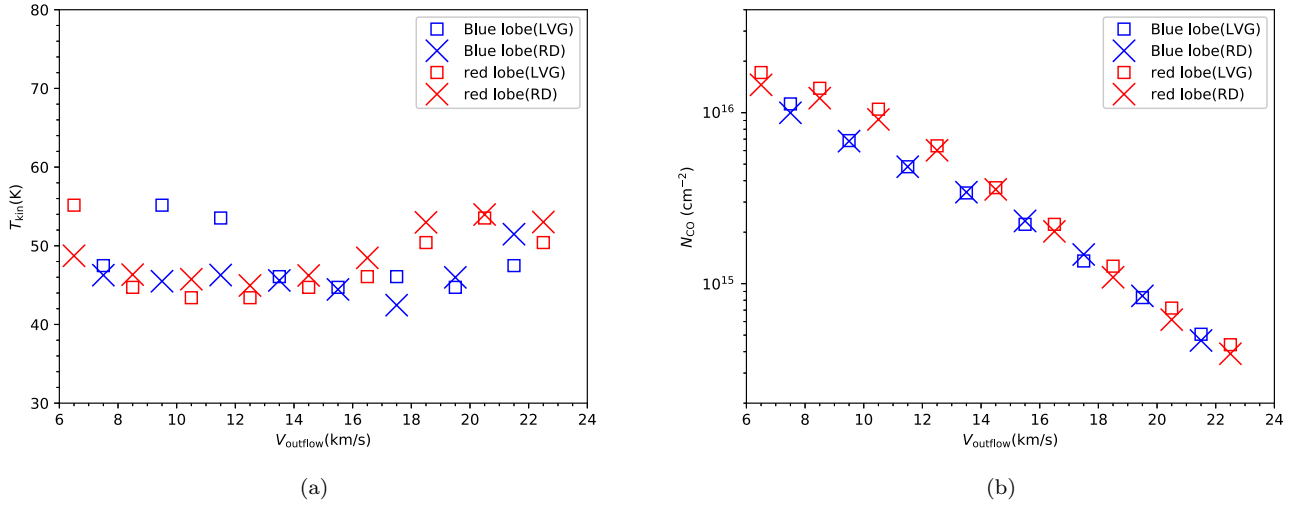
Figure 5. *T-V* and *N-V* diagrams of the G240 outflow, estimated from the rotation diagram analysis (blue "x" markers for the blue lobe and red "x" markers for the red lobe) and the LVG analysis (blue open squares for the blue lobe and red open squares for the red lobe).

22 km s^{-1}. We compared the model intensities with line intensities measured at several different positions, and found that the modeling results are similar to those represented in Figure 5. Thus, a systematic bias of position offsets was excluded.

(handwritten margin note in red): We performed RD and LVG analyses of the CO lines in different positions, and obtained similar T-V and N-V relations.

4. DISCUSSION

4.1. *Gas temperature*

Although the morphology and kinematics of molecular outflows have been widely studied, the driven mechanism of the outflowing gas is still unclear. Investigating the the *T-V* relation of molecular outflows would be helpful to address this question. Based on the constant CO 3-2/6-5 ratios, Yıldız et al. (2012) suggested that there is little or no temperature change with velocity in the outflow associated with low-mass protostars NGC 1333 IRAS 4A and 4B. With CO 2-1 and CO 3-2 observations, Su et al. (2012) performed an LVG analysis on the extremely high velocity outflow associated with the high-mass star-forming region G5.89-0.39 and found an increasing temperature with outflow velocity. In their works, assumptions for other outflow parameters (e.g. gas density, canonical CO fractional abundance and velocity gradient) were made to infer the *T-V* relations from only two CO lines, while these assumptions might not be necessarily valid. To more precisely determine the outflow properties, multi-line CO studies with sophisticated radiative transfer methods (e.g. LVG analysis) are needed. Recently, Lefloch et al. (2015) performed a multi-transition CO analysis on the outflow cavity of the intermediate-mass Class 0 pro-

tostar Cepheus E-mm and revealed an isothermal low-excitation outflow cavity with transitions of $J_{up} \leq 9$. Our analysis reveals that the G240 outflow, which is representative of a well-defined bipolar wide-angle molecular outflow in a $> 10^4 L_\odot$ star-forming region (Qiu et al. 2009), is approximately isothermal with a gas temperature of ~ 50 K. This isothermal state is similar to the behavior of outflows (traced by CO transitions of $J_{up} \leq 9$) associated with low-mass and intermediate-mass protostars (Yıldız et al. 2012; Lefloch et al. 2015), and the temperature of ~ 50 K is slightly lower than temperature constraints for outflows of low-mass protostars (van Kempen et al. 2009a; Yıldız et al. 2012) and intermediate-mass protostars (van Kempen et al. 2016). The derived outflow temperature is warmer than the previously adopted ~ 30 K (Qiu et al. 2009), which indicates that the physical parameters (mass, momentum, energy) of the G240 outflow calculated by Qiu et al. (2009) were underestimated by a factor of 1.32.

4.2. *Gas density and CO column density*

In the optically thin case, the CO column density N is related to the gas density n through the expression:

$$N = n \times \Delta V \times \frac{1}{dv/dr} \times X_{CO} \times f_b, \qquad (2)$$

where f_b is the beam filling factor, X_{CO} the [CO]/[H$_2$] abundance ratio, ΔV the velocity interval and dv/dr is the velocity gradient. The CO column density is degenerate with the beam filling factor, the velocity gradient and the abundance ratio. From $\sim \pm 7$ km s^{-1} to $\sim \pm$

(handwritten margin note in red, bottom): The morphology and kinematics of molecular outflows have been widely studied based on single spectral line observations. However, the physical conditions of the outflow gas are still not well constrained. In particular, how the physical conditions vary with the outflow velocity is poorly understood. 接下来，对已有工作的讨论要进一步展开，比如，Yildiz et al. (2012)是用的什么样的观测？得到多大速度范围内变化？等等。对Su et al. (2012)的讨论可以详细看看他们的工作在大质量outflow中是否首次，等等。这儿还应该加进最近我们发表在RAA的工作（Xie & Qiu 2018）。

首先，应该先指出N(CO)随V的明显变化。接着要讨论，如果X_CO不变化，就如大部分的工作假设的一个10^-4那样，那这个结果就表明beam averaged N(H2)随V明显的变化。再接着讨论beam filling factor的问题。在这里，应该想到，beam filling factor会不会对T-V关系产生影响？如果会或者不会，是否需要指出？

AASTeX G240   7

22 km s^{-1} with respect to the cloud velocity, the beam-filling factor decreases from ~ 0.5 down to ~ 0.2 (derived from source sizes of $\sim 20''$ to $\sim 10''$, see Figure 3 of Qiu et al. (2009)). The beam-averaged CO column density at the lowest flow velocity is 50 times larger than that at the highest flow velocity, whereas the beam filling factor is only 2.5 times larger. From the LVG analysis, the lower limit of the gas density is $\sim 10^5$ cm^{-3}, higher than or comparable to the critical density of each line at 50 K (9×10^3 cm^{-3}, 3×10^4 cm^{-3}, 3×10^5 cm^{-3} and 4×10^5 cm^{-3} for the CO 2-1, 3-2, 6-5 and 7-6 lines, respectively.). If the CO abundance and the velocity gradient do not vary much, the decrease of CO column density indicates that the gas density decreases with velocity, and that the gas density is $> 10^6$ cm^{-3} at the lowest flow velocity. The gas density limit is comparable to the density of the outflow cavity associated with Cepheus E-mm ($(1\text{-}8) \times 10^5$ cm^{-3}: Lefloch et al. 2015).

4.3. *The origin of the G240 outflow*

为什么不展开？

逻辑不对

Our analysis results reveal that the gas temperature of the outflow is relatively constant and that the outflow density decreases with outflow velocity. Such trends agree with the wind-driven model, while different temperature and density trends are predicted by other outflow models (Arce et al. 2007). Qiu et al. (2009) found that the kinematic structure and morphology of the G240 outflow can also be qualitatively interpreted by the wide-angle wind-driven model. Thus, we conclude that the G240 outflow is mainly driven/entrained by a wide-angle wind, which itself may resemble the accretion-driven wide-angle winds (X-wind or disk winds: Shang et al. 2006; Pudritz et al. 2006) associated with low-mass YSOs, and we further suggest that disk-mediated accretion may exist in the formation of high-mass stars up

to late-O types. We noticed that there are faint bow-shaped H$_2$ features near the source IRAS 07427-2400 (Kumar et al. 2002), indicating that the jet bow shock entrainment may also contribute to the G240 outflow. Mid-J CO observations with higher resolution (e.g., with ALMA) are needed to study these suspicious bow shock features in detail. It should be noted that most existing outflow models can only explain typical parameters of outflows driven by low-mass YSOs, and high-mass outflow models are necessary to quantitatively explain the physical conditions of outflows associated with high-mass YSOs. Statistical analyses of high-mass outflows are also essential for us to better understand the driven mechanism of massive outflows and the forming process of high-mass stars.

这种讨论的依据不充分，对这个文章的意义也不大

5. SUMMARY

Using the APEX CO 3-2, 6-5 and 7-6 observations and the complementary CO 2-1 data, we have presented the first CO multi-transition study toward the molecular outflow of the high-mass star-forming region G240. The parsec-sized, bipolar, and high velocity outflow is clearly revealed by the CO 3-2, 6-5 and 7-6 emissions. For both lobes the outflow is approximately isothermal with a temperature of ~ 50 K. The outflowing gas is thermalized with a H$_2$ density higher than $n \sim 10^5$ cm^{-3}. The CO column density of the outflow decreases with gas velocity. The gas density might decrease with outflow velocity if the CO abundance and velocity gradient remain relatively constant. The isothermal state and the decreasing gas density indicate that the wide-angle wind-driven entrainment is the dominant driving mechanism of the G240 outflow. This finding further suggests that disk-accretion can be responsible for the formation of high-mass stars even more massive than early B-type stars.

REFERENCES

Arce, H. G., Shepherd, D., Gueth, F., et al. 2007, Protostars and Planets V, 245

Banerjee, R., & Pudritz, R. E. 2006, ApJ, 641, 949

Beuther, H., Schilke, P., Sridharan, T. K., et al. 2002, A&A, 383, 892

Beuther, H., Schilke, P., Gueth, F., et al. 2002, A&A, 387, 931

Caswell, J. L. 1997, MNRAS, 289, 203

Caswell, J. L. 2003, MNRAS, 341, 551

Choi, Y. K., Hachisuka, K., Reid, M. J., et al. 2014, ApJ, 790, 99

Frank, A., Ray, T. P., Cabrit, S., et al. 2014, Protostars and Planets VI, 451

Goldsmith, P. F., & Langer, W. D. 1999, ApJ, 517, 209

Heyminck, S., Kasemann, C., Güsten, R., de Lange, G., & Graf, U. U. 2006, A&A, 454, L21

Hughes, V. A., & MacLeod, G. C. 1993, AJ, 105, 1495

Kasemann, C., Güsten, R., Heyminck, S., et al. 2006, Proc. SPIE, 6275, 62750N

Kumar, M. S. N., Bachiller, R., & Davis, C. J. 2002, ApJ, 576, 313

Kumar, M. S. N., Fernandes, A. J. L., Hunter, T. R., Davis, C. J., & Kurtz, S. 2003, A&A, 412, 175

Lee, C.-F., Mundy, L. G., Reipurth, B., Ostriker, E. C., & Stone, J. M. 2000, ApJ, 542, 925

Lee, C.-F., Stone, J. M., Ostriker, E. C., & Mundy, L. G. 2001, ApJ, 557, 429

Lee, C.-F., Mundy, L. G., Stone, J. M., & Ostriker, E. C. 2002, ApJ, 576, 294

Lefloch, B., Gusdorf, A., Codella, C., et al. 2015, A&A, 581, A4

Li, G.-X., Qiu, K., Wyrowski, F., & Menten, K. 2013, A&A, 559, A23

Machida, M. N., Inutsuka, S.-i., & Matsumoto, T. 2008, ApJ, 676, 1088-1108

MacLeod, G. C., Scalise, E., Jr., Saedt, S., Galt, J. A., & Gaylard, M. J. 1998, AJ, 116, 1897

Masson, C. R., & Chernin, L. M. 1993, ApJ, 414, 230

Maud, L. T., Moore, T. J. T., Lumsden, S. L., et al. 2015, MNRAS, 453, 645

Migenes, V., Horiuchi, S., Slysh, V. I., et al. 1999, ApJS, 123, 487

Pudritz, R. E., Rogers, C. S., & Ouyed, R. 2006, MNRAS, 365, 1131

Pudritz, R. E., Ouyed, R., Fendt, C., & Brandenburg, A. 2007, Protostars and Planets V, 277

Qiu, K., Zhang, Q., Wu, J., & Chen, H.-R. 2009, ApJ, 696, 66

Qiu, K., Zhang, Q., Menten, K. M., et al. 2014, ApJL, 794, L18

Raga, A., & Cabrit, S. 1993, A&A, 278, 267

Ren, J. Z., Liu, T., Wu, Y., & Li, L. 2011, MNRAS, 415, L49

Sakai, N., Nakanishi, H., Matsuo, M., et al. 2015, PASJ, 67, 69

Shang, H., Allen, A., Li, Z.-Y., et al. 2006, ApJ, 649, 845

Shepherd, D. S., Watson, A. M., Sargent, A. I., & Churchwell, E. 1998, ApJ, 507, 861

Shu, F. H., Ruden, S. P., Lada, C. J., & Lizano, S. 1991, ApJL, 370, L31

Shu, F. H., Najita, J. R., Shang, H., & Li, Z.-Y. 2000, Protostars and Planets IV, 789

Su, Y.-N., Liu, S.-Y., Chen, H.-R., & Tang, Y.-W. 2012, ApJL, 744, L26

Trinidad, M. A. 2011, AJ, 142, 147

van der Tak, F. F. S., Black, J. H., Schöier, F. L., Jansen, D. J., & van Dishoeck, E. F. 2007, A&A, 468, 627

van Kempen, T. A., van Dishoeck, E. F., Güsten, R., et al. 2009, A&A, 501, 633

van Kempen, T. A., van Dishoeck, E. F., Güsten, R., et al. 2009, A&A, 507, 1425

van Kempen, T. A., Hogerheijde, M. R., van Dishoeck, E. F., et al. 2016, A&A, 587, A17

Wu, Y., Wei, Y., Zhao, M., et al. 2004, A&A, 426, 503

Wu, Y., Zhang, Q., Chen, H., et al. 2005, AJ, 129, 330

Yıldız, U. A., Kristensen, L. E., van Dishoeck, E. F., et al. 2012, A&A, 542, A86

Zhang, Q., Hunter, T. R., Brand, J., et al. 2001, ApJL, 552, L167

APPENDIX

A. SPECTRAL LINE FLUX DISTRIBUTIONS
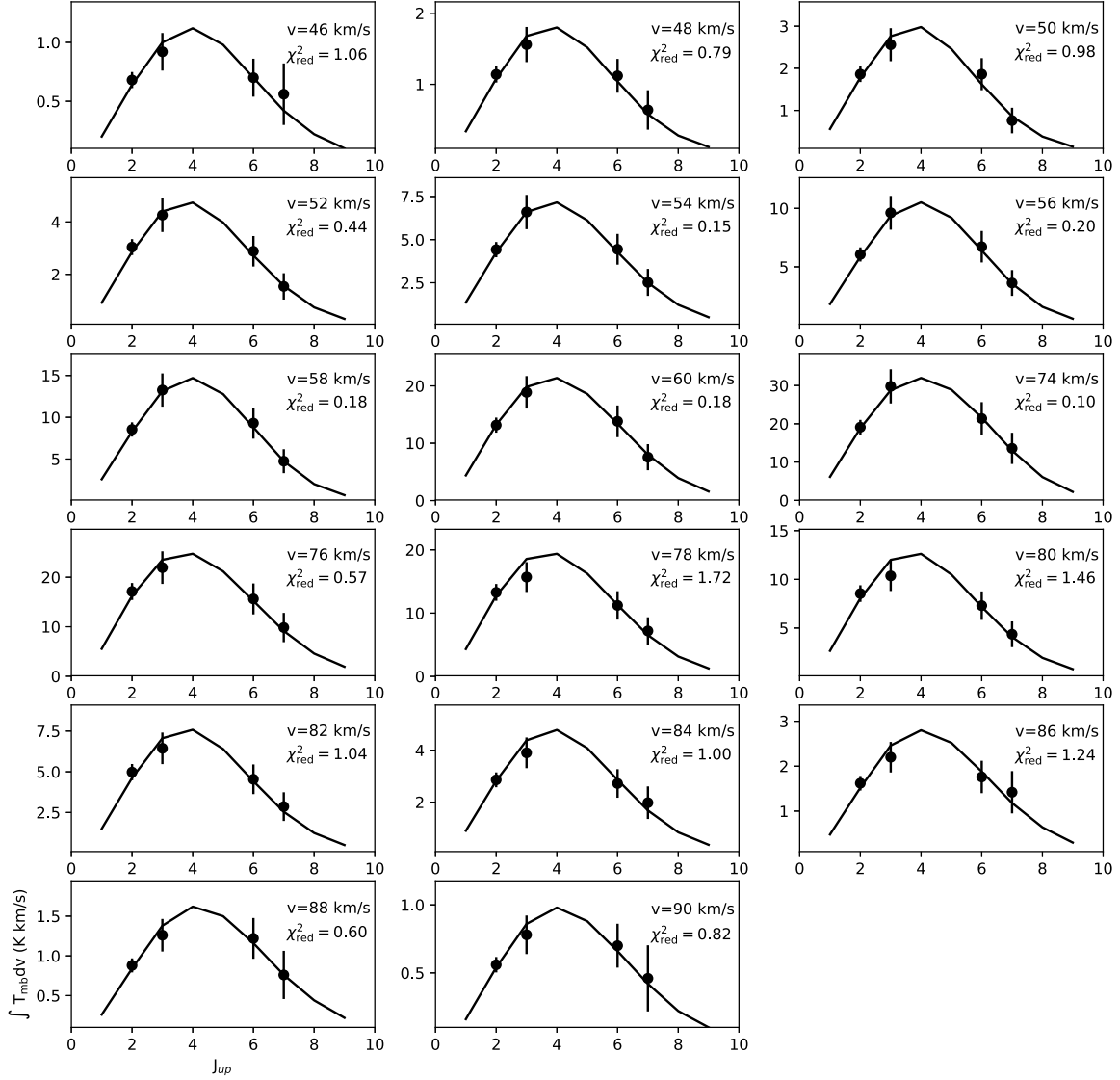
Figure A1. Observed line fluxes compared with the LVG computations in each 2 km/s bin. The black solid circles show the observed data with error bars. The black solid lines refer to the best fits. The $\chi^2_{\rm red}$ of the best fitting results and the outflow velocities are shown in each panel.